Ceramics International xxx (xxxx) xxx

Contents lists available at ScienceDirect

Ceramics International

journal homepage: www.elsevier.com/locate/ceramint

Understanding the effect of temperature on the crystallization of Eu^{3+}:YPO_4 nanophosphors prepared by MW-assisted method

Enrico Paradisi [a], Cecilia Mortalò [b,*], Valentina Zin [b], Silvia Maria Deambrosis [b], Mauro Zapparoli [c], Enrico Miorin [b], Cristina Leonelli [a]

[a] Department of Engineering "Enzo Ferrari" (DIEF), University of Modena and Reggio Emilia, Via P. Vivarelli 10, Modena, 41125, Italy
[b] Institute of Condensed Matter Chemistry and Technologies for Energy (ICMATE), National Research Council of Italy (CNR), Corso Stati Uniti 4, Padova, 35127, Italy
[c] Interdepartmental Research Centre "CIGS", University of Modena and Reggio Emilia, via Campi 213/A, Modena, 41125, Italy

ARTICLE INFO

Handling Editor: P. Vincenzini

Keywords:
Eu^{3+}:YPO_4 nanophosphors
MW-Assisted synthesis
Crystallization
Temperature effect
Tuned morphology

ABSTRACT

The influence of the reaction temperature on the crystallization process of Eu^{3+}:YPO_4 (5 % mol of Eu^{3+}) luminescent materials was investigated under MW-assisted heating, in aqueous media and without the use of organic templating agents. X-ray diffraction (XRD), Fourier transform infrared (FT-IR) spectroscopy, Raman spectroscopy and transmission electron microscopy (TEM) analyses were employed to investigate the crystallization and morphological evolution. The syntheses were conducted via a MW-assisted hydrothermal method by heating at temperatures from 120 to 240 °C with a holding time of 20 min. The majority of the resulting powders were observed to be amorphous at 120 and 140 °C, exhibiting only minimal evidence of very small crystallites. Conversely, crystalline Eu^{3+}:YPO_4 powders with a single-phase tetragonal *Xenotime-Y* structure were obtained at 160 °C, in the form of nanosticks aggregating into nanobundles. It was found that a crystallization threshold for the formation of nanocrystalline Eu^{3+}:YPO_4 materials exists between 140 °C and 160 °C. As the reaction temperature was increased, a dehydration process occurred, resulting in the gradual disappearance of the residual amorphous phase. This resulted in the formation of fully crystalline nanoparticles at 200 °C. At this temperature, the coalescence of nanobundles into nanorods was observed, and this morphology became increasingly defined as the synthesis temperature was increased up to 240 °C. These findings highlight the pivotal role of temperature in the crystallization of these nanophosphors in an aqueous media at pH 7, thereby addressing a gap in the existing scientific literature.

1. Introduction

The research on luminescent nanomaterials is a subject of considerable interest within the academic community, given the intriguing properties of these materials and their potential applications across a range of fields [1]. Typically, these materials comprise a host crystal lattice with guest atomic impurities, named dopants, which are essential for the observed luminescence. These dopants often belong to the large family of rare earths (RE) [2]. The existence of a multitude of host matrices, each capable of accommodating different dopants in a wide range of concentrations, has prompted researchers to develop a vast array of luminescent materials, each tailored to emit at a specific wavelength or to possess other beneficial properties [3]. Among the various host matrices, rare earth oxides (RE_2O_3) [3,4], vanadates ($REVO_4$) [1,5,6] and phosphates ($REPO_4$) [6] have been the subject of extensive research due to their ability to readily accommodate RE^{3+} cations within their structure, which endows these compounds with luminescent properties. In particular, RE^{3+} doped YPO_4 materials have been demonstrated to display bright, efficient and long-lasting luminescence, high durability and chemical stability, and excellent mechanical and thermal properties, particularly in their anhydrous crystal structures, namely the tetragonal *Xenotyme-Y* and monoclinic *Monazite* phases [6]. The exceptional properties of *Xenotyme* and *Monazite* are directly attributable to their anhydrous crystal structures. This is evidenced by the fact that water molecules embedded in (partially) hydrate forms, such as *Rhabdophane* ($REPO_4 \bullet 0.8H_2O$) [7] and *Churchite* ($REPO_4 \bullet 2H_2O$) [8], are responsible for reduced quantum efficiency and luminescence intensity [9–11]. Furthermore, the dimensions of the nanoparticles and their morphology have been demonstrated to impact the photoluminescence properties of the material [13–15]. Consequently,

* Corresponding author.
E-mail address: cecilia.mortalo@cnr.it (C. Mortalò).

https://doi.org/10.1016/j.ceramint.2024.12.144
Received 11 October 2024; Received in revised form 25 November 2024; Accepted 9 December 2024
Available online 10 December 2024

considerable efforts have been conducted to develop synthetic techniques for the production of the desired compounds with the optimal crystal structure, morphology, and particle size [16]. To date, a substantial number of wet-chemistry methods have been developed for the preparation of RE^{3+}-doped YPO_4 nanopowders, including hydrothermal [15,17,18], co-precipitation [13,19], polyol [20] and sol-gel [21–24] techniques. The structure, size, shape and morphology of the powders can be modified by altering the various synthesis parameters, including the pH value, precursors and reaction temperature [16]. The utilisation of templating agents typically resulted in the formation of hydrated *Rabdophane* hexagonal prisms [15,25,26], whereas the tetragonal *Xenotime-Y* phase was generally obtained without additives, except in certain instances where neutral pH conditions facilitated the formation of the tetragonal phase even in the presence of a templating agent [27, 28]. The size and shape of the tetragonal phase are also influenced by the percentage of dopant used [29], synthesis time [17,30], reaction temperature [31], annealing temperature [21], and the preparation method [33]. Among these, microwave (MW) assisted methods have recently emerged as a rapid, efficient and reliable method for the preparation of luminescent inorganic materials [34,35]. The rapid and uniform heating provided by MW generally results in shorter reaction times and a uniform size and shape distribution of the nanoparticles. Furthermore, the utilisation of MW can facilitate alloy phase transformation and stabilisation in materials [36,37], and support processes conducted under vacuum conditions [38,39] or in the solid state [40]. In the case of $REPO_4$, some kinetic studies were conducted using a microwave-assisted method to investigate the formation of the *Rabdophane* phase from the system 0.53 $LaPO_4$ – 0.47 YPO_4 • (n H_2O) and its subsequent transformation into *Monazite* [41]. Moreover, Wang et al. described the utilisation the use of templating agents to obtain uniform spherical microparticles of $REPO_4$ or RE-doped YPO_4, through microwave heating at 180 °C for 2 h, and the investigation of phase transformation through alterations in the type of lanthanide or the ratio of reagents [42]. The utilisation of microwaves was deemed imperative for the prevention of anisotropic growth, as the expeditious heating process would preclude the occurrence of this mechanism. The same research group proceeded to synthesize YPO_4 doped with varying RE cations for the assessment of luminescence properties and the potential applications in anticounterfeiting inks [43]. Rodriguez Liviano et al. successfully produced well-defined lenticular nanoparticles with precisely controlled size at extremely low reaction temperatures (approximately 120 °C) by modifying the ratio of reactants and employing $Y(acac)_3$ as the yttrium precursor [44]. Majeed et al. observed a distinctive morphology of Eu-doped YPO_4 nanopowders, which were obtained by a rapid MW-assisted synthesis under acidic conditions at a relatively low temperature, resulting in highly dispersible nanobundles with potential biomedical applications [45]. A comparable morphology was also identified by Vanetsev et al. in a comprehensive investigation of the impact of specific experimental parameters (including reagent ratio, synthesis time and pH) on the crystalline phase, size and morphology of undoped YPO_4 nanoparticles [46]. Nanobundles with a *Xenotime-Y* crystalline phase were obtained at 200 °C, using equimolar amounts of reactants, a natural pH and a reaction time of 1 h. The same morphology was observed also in Eu^{3+}:YPO_4 prepared by a glycine-assisted hydrothermal method by Yang et al. at 150 °C [47]. Recently, we have successfully synthesized Eu^{3+}:YPO_4 nanocrystals with a well-defined rice-like morphology by a microwave-assisted hydrothermal method at 200 °C and with reaction times as short as 3–5 min [48].

While numerous papers have reported studies on the impact of the reaction time and other experimental parameters (e.g. pH, reagents and their relative amounts, additives) on the crystallization and morphology of Eu^{3+}:YPO_4 powders [14,15,46,48], to the best of our knowledge, only a few studies have focused on the effect of the reaction temperature [31, 32,48]. Liu et al. examined the impact of temperature on the particle size and morphology of undoped YPO_4 and Eu^{3+}:YPO_4 materials (5 % mol of Eu) prepared via a conventional hydrothermal method. Upon heating from 80 to 200 °C for 12 h under acidic conditions, irregularly shaped nanopowders and Xenotime-Y tetragonal structures were obtained. An increase in particle size and a contraction in volume were observed with an increase in temperature [31]. Cybinska obtained different outcomes by preparing powders with an identical Eu content and utilising a comparable hydrothermal methodology and experimental conditions. Indeed, Eu^{3+}:YPO_4 powders exhibiting disparate sizes within the micrometre range and displaying a combination of disc-like and octahedral morphologies were obtained by subjecting the samples to a heating process for a duration of 10 h at temperatures spanning the range of 120–240 °C. The pure tetragonal phase was obtained at all temperatures, with no variation in the lattice parameters reported in the paper [32]. A MW-assisted hydrothermal method was recently employed under neutral conditions. It was observed that an increase in temperature from 200 to 240 °C resulted in a change in the morphology of Eu^{3+}:YPO_4 nanopowders (with 5 % mol of Eu) from a mixed morphology to an elongated rod-like monodispersed morphology [48]. However, the temperature range was limited to 200–240 °C, and a comprehensive investigation into the impact of reaction temperature on the crystallization mechanism was not conducted. In order to gain a deeper understanding of the optical properties of these luminescent materials and their practical applications, it is essential to ascertain the crystallization behaviour of the powders and the role of temperature in controlling the size and morphology. The objective of this study is to gain insight into the role of temperature in the crystallization process under neutral conditions and to propose a mechanism for crystal formation, thereby addressing a gap in the existing literature. To this end, Eu^{3+}:YPO_4 powders with 5 mol% Eu as the optimal dopant concentration [29] were prepared by microwave-assisted hydrothermal conditions without organic templates or solvents, in the temperature range of 120–240 °C and with a fixed reaction time of only 20 min. A series of analytical techniques, including X-Ray Diffraction (XRD), Raman, Infrared spectroscopy (FT-IR) and Transmission Electron Microscopy (TEM), were employed to assess the structural and morphological alterations of the prepared powders. Additionally, Raman analysis was conducted to ascertain the optical properties of the materials.

2. Experimental

2.1. synthesis of Eu^{3+}:YPO_4 nanopowders

The precursors $Y(NO_3)_3{\cdot}6H_2O$ (99.8 %, Sigma-Aldrich), $Eu(NO_3)_3{\cdot}5H_2O$ (99.9 %, Sigma-Aldrich), and KH_2PO_4 (≥98.0 %, Sigma-Aldrich) were employed without further purification for the preparation of Eu^{3+}:YPO_4 (5 % mol of Eu) nanopowders. The syntheses were conducted in accordance with the methodology described in Ref. [48]. The experimental conditions and the names of the prepared samples are provided in Table 1. Samples **PHO-RT_1** and **PHO_RT** were obtained after precipitation at room temperature, at pH values of 1 and 7, respectively, and without microwave heating. The MW-assisted hydrothermal treatments were conducted at varying temperatures for a duration of 20 min, with a power of 800 W in an ETHOS TOUCH apparatus (Milestone s.r.l., Sorisole, Italy). All powders were subjected to multiple washes with deionised water to eliminate any residual by-products, after which they were subjected to centrifugation (ALC Centrifuge, PK110, **ALC INTERNATIONAL S.r.l, 20093 Cologno Monzese, MI, Italy**). The resulting white powders were obtained after drying at 70 °C for 24 h, with a reaction yield of approximately 95 %.

2.2. Methods

X-ray diffraction (XRD) patterns were collected using an Empyrean series III Multicore diffractometer (Malvern PANAlytical, Malvern, UK), equipped with a PIXcel3D detector, utilising Cu-kα radiation (λ = 1.5405 Å) from a Cu LFF HR source with a b-Ni filter. The experiments were conducted at room temperature and at 40 kV and 40 mA, within

Table 1
Experimental conditions, cell parameters, crystallite sizes and root-mean-square (r.m.s.) microstrain values (calculated by Rietveld refinement) of the crystallized Eu^{3+}:YPO_4 powders prepared by MW-assisted heating at different temperatures.

Sample	T (°C)	*a* (Å)	*c* (Å)	Crystallite size (nm)	r.m.s. microstrain
PHO_RT_1	r.t.	/	/	/	/
PHO_RT	r.t.	/	/	/	/
PHO_120	120	/	/	/	/
PHO_140	140	/	/	/	/
PHO_160	160	6.9324 ± 0.0012	6.0328 ± 0.005	37 ± 3	$9.3 \cdot 10^{-6}$
PHO_180	180	6.9299 ± 0.0011	6.0312 ± 0.004	35 ± 3	$5 \cdot 10^{-5}$
PHO_200[a]	200	6.9286 ± 0.0011	6.0303 ± 0.003	32 ± 2	0.001
PHO_220	220	6.9302 ± 0.0009	6.0274 ± 0.004	28 ± 2	0.0025
PHO_240[a]	240	6.9202 ± 0.0013	6.0212 ± 0.004	28 ± 1	0.0027

[a] Data from ref. [48].

the 5–80° 2θ range, with a step size of 0.039° and a time step of 0.5 s. The X-ray beam was filtered using a primary mask of 14 mm and a secondary mask of 6 mm, a primary and secondary slit of ¼ cm, and a 0.03 cm primary Soller slit and a 0.04 cm secondary Soller slit. The phase identification was conducted using the X'pert HighScore Plus® software with the JCPDS database. The reference pattern employed to identify the xenotime-(Y) tetragonal structure as the sole Eu:YPO_4 phase present in our samples was JCPDS card 00-011-0254. The collected spectra were processed with the Maud v.2.9 software [49,50] in order to estimate the lattice parameters, crystalline domain sizes and microstrains. This was achieved through the application of the Rietveld analysis to the peak broadening and position. The crystallite sizes were calculated by taking the mean between the two directions in elongated particles, namely length and thickness. Rietveld processing models of the MAUD software were employed to ascertain the dimensions of spherical coherent scattering domains (or, in the form of "composite" domains, as postulated by Nicolae Popa) and a number of root-mean-square microdeformation values [51]. In the case of anisotropic crystallite shapes, Popa's model has been employed, as it accounts for the size-broadened profile resulting from the log-normal size distribution of spherical crystallites. This enables the estimation of the radius of an apparent crystallite, which serves as an approximation to real crystallites and their distribution [52].

Fourier transform infrared (FT-IR) attenuated total reflection (ATR) spectra were acquired using a VERTEX 70V Bruker (Billerica, MA, USA) spectrophotometer. The instrument was equipped with a Platinum ATR unit with a diamond crystal (refractive index of 2.4), a GLOBAR source, and a MCT Mid-Band detector. The spectra were acquired in transmittance mode, utilising a range of 4000 to 600 cm^{-1}, a spectral resolution of 2 cm^{-1}, and 32 scans. The data analysis was conducted using Origin™ software. All spectra were normalised to the intensity range 0–1, facilitating a more straightforward comparison.

Raman measurements were conducted using a LabRAM HR Evolution Raman microscope (Horiba Ltd., 2 Miyanohigashi, Kisshoin, Minami-ku Kyoto, 601–8510 Japan). The laser source employed was a 532 nm Nd-YAG with a maximum output power of 100 mW. The microscope employed was an Olympus BXFM-ILHS, equipped with 5x, 10x, 100x, 50x LWD, and 100x LWD objectives. The detector was a charge-coupled device (CCD) front-illuminated open electrode with a multi-pin phase detector, exhibiting a spectral range of 200–1100 nm, multiple Peltier cooling, and a 1024 x 256 x 16 matrix. Spectra were acquired utilising a laser power of 1 %, a 100x objective, and acquisitions of 3 s with 5 accumulations. The data were then elaborated with Origin™ software. All spectra were normalised to the intensity range 0–1, facilitating easier comparison. The Raman shift scale was transformed into a wavelength (λ) scale using the following equation:

$$\lambda\ (nm) = \frac{1}{Abs.\ wavenumber\ (cm^{-1})} \times 10^7$$

Absolute wavenumber is obtained by subtraction of observed Raman shifts from the absolute wavenumber corresponding to the laser wavelength (532 nm). Since:

$$Abs.\ wavenumber\ (cm^{-1}) = \frac{1}{\lambda\ (nm)} \times 10^7$$

In this case

$$Abs.\ wavenumber\ (cm^{-1}) = \frac{1}{532} \times 10^7 = 18796.99\ cm^{-1}$$

Therefore, the wavelength data are obtained as follows:

$$Wavelength\ (nm) = \frac{1}{Abs.\ wavenumber\ (cm^{-1})} = \left(\frac{1}{(18796.99 - X)}\right) \times 10^7$$

Where X = Observed Raman shifts.

Representation of data for a precise graphical correspondence between wavelength and wavenumbers required selecting the "reciprocal" scale type on the Origin™ program.

TEM. A high-resolution scanning/transmission electron microscope (S/TEM) (Thermo Scientific™, Waltham, MA, USA, Talos™ F200S) equipped with energy dispersive X-ray spectroscopy (EDS) and operating at 200 kV acceleration voltage was used for TEM analyses. To prepare the samples, aqueous suspensions of the powders were sonicated for 15 min at room temperature. Therefore, 200 mesh copper microscope grids coated with carbon were immersed in the sonicated suspensions. Finally, the samples were dried under IR irradiation prior to analysis. The mean dimensions and particle size distributions were determined by measuring a minimum of 200 individual particles in the TEM micrographs using ImageJ software (version 1.53t) and fitting them with normal or log-normal functions using the Origin™ program.

3. Results and discussion

3.1. XRD and FT-IR analysis

The X-ray diffraction (XRD) patterns of all the samples synthesized in this study are presented in Fig. 1. XRD is a powerful and versatile technique that can be employed to study the microstructure of materials and evaluate their evolution as a function of synthesis or treatment parameters [53]. The collected patterns display broad and indistinct peaks in the spectrum of the samples precipitated at room temperature (both at pH = 1 and 7), as well as in those of the samples prepared at pH = 7 and heated at 120 °C and 140 °C (Fig. 1a). This suggests that the initial precipitation of Eu^{3+}:YPO_4 at room temperature results in the formation of a predominantly amorphous phase. Further heating at 120 °C or 140 °C does not significantly promote extensive crystallization. An increase in temperature to 160 °C results in a significant change in crystallinity (Fig. 1b). This is evidenced by the emergence of sharp and well-defined peaks, which are characteristic of the *Xenotyme-Y* phase with a tetragonal structure (JCPS: 00–011–0254) and space group $I4_1/amd$. This phase corresponds to anhydrous yttrium phosphate (V). Similarly, Majeed et al. [45], and Yang et al. [47], obtained Eu-doped YPO_4 nanopowders with a tetragonal structure after 30 min of heating at 150 °C by using a MW-assisted method under acidic conditions and after 24 h by a glycine-assisted hydrothermal synthesis, respectively.

As illustrated in Fig. S1, the formation of the crystalline structure is accompanied by the persistence of a residual disordered or amorphous phase, which is observed in samples produced at temperatures below 160 °C. Indeed, it can be observed that the background of the spectrum collected from the **PHO_160** sample displays a wave-like trend

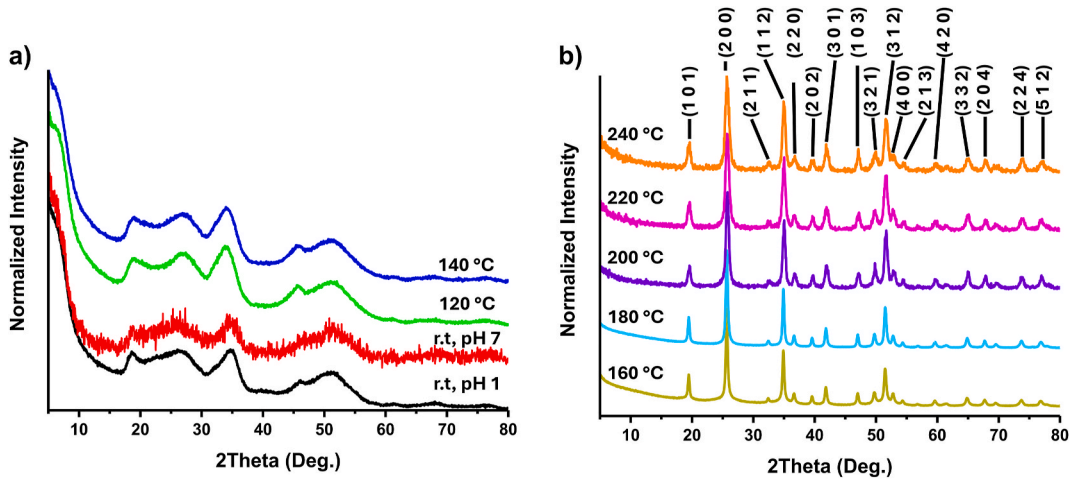

Fig. 1. XRD patterns of Eu^{3+}:YPO_4 samples obtained (**a**) at room temperature and by a MW-assisted heating at 120 and 140 °C and (**b**) at 160, 180, 200, 220 and 240 °C.

(highlighted with a red line in Fig. S1) that is similar to the shape of the spectrum of the **PHO_140** sample. This indicates the coexistence of two distinct phases, namely amorphous and crystalline, within the same material. Indeed, the Rietveld refinement methodology revealed the presence of an amorphous phase in samples **PHO_160** and **PHO_180**, but not in samples obtained at temperatures exceeding 200 °C. In fact, in samples obtained at higher temperatures, the presence of a linear background, which can be easily calculated, excludes the formation of the amorphous phase. It can therefore be assumed that the crystallization process is strongly influenced by the reaction temperature, with an incipient crystallization point occurring at around 160 °C. Indeed, at pH = 7, an increase in temperature up to 160 °C leads to the development of the crystalline phase as an evolution of the previous amorphous phase. A further increase up to 200 °C improves the crystallinity, as evidenced by a decrease in the signal of the amorphous phase, which allows for the emergence of a background with a pseudolinear trend. No further improvements in crystallinity were observed at temperatures above 200 °C (Fig. 1b). Table 1 shows the crystal lattice parameters of the identified *Xenotime-Y* phase for crystalline samples, spanning from **PHO_160** to **PHO_240**. In alignment with our prior findings [48], it can be observed that a slight decrease in both lattice parameters *a* and *c* occurs as the treatment temperature rises, resulting in a contraction of the cell volume. Furthermore, in contrast to the findings of Cybińska [32] and Liu et al. [31], who studied Eu^{3+}-doped and undoped YPO_4 nanopowders prepared via a conventional hydrothermal method, the average crystallite sizes calculated by Rietveld refinement were observed to decrease with increasing temperature. This behaviour is likely attributable to the dissolution, crystallization and dehydration processes occurring at elevated temperatures, which result in the formation of denser crystals, as also observed by Vanetsev et al. [46]. Since the Rietveld method takes into account both the main sources of physical line broadening in XRD patterns, namely finite crystallite size broadening and microstrain broadening, the root mean square (r.m.s.) microstrain values are also given in Table 1 for the samples analysed. The Rietveld method accounts for the primary sources of physical line broadening in XRD patterns, namely finite crystallite size broadening and microstrain broadening. Consequently, the root mean square (r.m.s.) microstrain values are also provided in Table 1 for the samples under analysis. The term 'microstrain' is defined as the root mean square of the variations in lattice parameters observed across a given sample. These variations are a consequence of non-uniform lattice distortions, faults, dislocations, antiphase domain boundaries and grain surface relaxation. The strain contribution to peak broadening is caused by the non-uniform displacements of atoms with respect to their reference lattice positions [6]. It can be observed that the microstrain increases with the treatment temperature, indicating that the decrease in crystallite size leads to the loss of long-range order domains and the increase in lattice distortion. The absence of extra peaks in the XRD spectra shows that there are no unwanted secondary phases or by-products in the materials produced [54].

The FT-IR spectra of all Eu^{3+}:YPO_4 samples are presented in Fig. S2 of the supporting information file. Some selected spectra are displayed in Fig. 2 as full spectra, with the intensity normalised to a range of 0–1. In the region between 4000 and 2500 cm^{-1}, the characteristic O-H stretching of water is observed for all samples. Furthermore, the smaller peak at approximately 1630 cm^{-1}, which is characteristic of the H-O-H bending, is also detected [18,46]. This indicates that all samples exhibit some degree of hydration, which is consistent with the fact that all syntheses are conducted in aqueous media. However, the intensities of these signals decrease with increasing reaction temperature (as illustrated graphically by the arrows in Fig. 2) and become negligible in samples obtained at 220 and 240 °C (Fig. S2).

In the 1250 to 600 cm^{-1} region the typical P-O antisymmetric

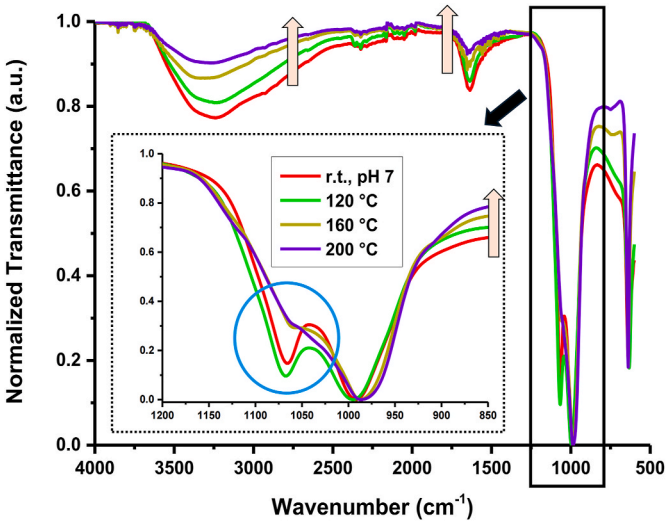

Fig. 2. FT-IR spectra of some selected synthesized samples (red line: as-precipitated sample obtained at pH = 7; green line: sample obtained at 120 °C; olive line: sample obtained at 160 °C; violet line: sample obtained at 200 °C). **Inset:** magnification of the part of the FT-IR spectra between 1300 and 600 cm^{-1} to highlight the P-O stretching region. (For interpretation of the references to colour in this figure legend, the reader is referred to the Web version of this article.)

stretching (≈1000 cm^{-1}) and the antisymmetric bending of the O-P-O group (≈630 cm^{-1}) can be seen [18,46,55]. As illustrated in the inset of Fig. 2 (indicated by a blue circle), the band centred at around 1000 cm^{-1} is resolved into two distinct bands (one at ≈ 1060 cm^{-1} and one below 1000 cm^{-1}) in the spectra of the amorphous samples (red and green lines). On the other hand, the spectra of the crystalline **PHO_160** and **PHO_200** samples exhibit a single, shoulder-shaped main band below 1000 cm^{-1}. As reported by Garrido Hernández et al., the peak observed below 1000 cm^{-1} is considered to be diagnostic of the tetragonal phase of Eu^{3+}:YPO_4 and is typical of nanopowders with a low degree of hydration. In contrast, the absorption band at ≈ 1060 cm^{-1} is attributed to amorphous materials and/or a high degree of hydration, as it corresponds to the P-OH bond [18]. Similar differences between the stretching bands of the PO_4^{3-} group were observed by Farida et al. [56]. These findings indicate that the reaction temperature influences the degree of hydration of these materials, which is consistent with the observations made by Wang et al. in analogous compounds prepared via conventional hydrothermal synthesis, resulting in a lower energy stretching mode of the phosphate groups [57]. Consequently, an elevated reaction temperature correlates with enhanced crystallinity of the samples, which exhibit a reduced number of water molecules or free OH groups, ultimately leading to the elevated luminescence [12].

3.2. Raman analysis

Raman investigations were carried out to complement and support the results of the XRD and infrared analyses. Fig. S3 of the Supporting Information file illustrates the Raman spectra of Eu^{3+}:YPO_4 samples within the range of 200–1200 cm^{-1}. The vibrational modes of the phosphate ions (i.e., A_{1g}, B_{1g}, E_g and B_{2g}) are more evident in the spectra of samples obtained at temperatures ≥160 °C. However, their intensity is significantly attenuated with respect to the undoped materials [17,31,58,59]. This behaviour is related to the effect of europium incorporation in the YPO_4 host, as previously reported in the literature [60–62]. Consequently, the recording range of the Raman spectra was extended, resulting in the observation of pronounced peaks within the 1000–5000 cm^{-1} region, which is frequently overlooked in the reporting of Raman spectra of doped yttrium phosphates (Fig. 3) [63].

Fig. 3a illustrates the Raman spectra of the samples obtained at room temperature and at 120 and 140 °C, while Fig. 3b depicts the spectra of the samples obtained at a temperature range of 160–240 °C. The signals observed in the Raman spectra are attributed to the photoluminescence (PL) of the samples and correspond to the characteristic PL bands of the Eu^{3+} ions, which are typically observed in the orange-red region of the PL emission spectra of the Eu^{3+}:YPO_4 materials [17,48,63]. No shift in the position of the bands is observed between the samples. The observation of photoluminescence signals in the Raman spectrum is a common occurrence [64,65]. This is because Raman scattering and PL are two distinct physical processes arising from the same stimulus, namely laser excitation [66,67]. Usually, the PL of a sample is regarded as a potential limitation when interpreting the Raman spectrum [68]. However, there are instances where it is possible to examine the characteristics of the sample in PL and Raman simultaneously [65,69]. This appears to be the case for Eu^{3+}:YPO_4, as the PL and Raman signals do not overlap. As illustrated in Fig. S3, only very weak lattice vibrations (i.e. "real" Raman signals) are observed below 1000 cm^{-1}. Furthermore, the bending and stretching Raman modes of water are evident, as indicated by the grey dashed lines in Fig. 3 [70]. The appearance of PL peaks in Raman spectra is the initial indication of Eu^{3+} doping in the YPO_4 lattice, given that the Raman spectrum of undoped YPO_4 is unperturbed in the region 1000 to 4000 cm^{-1} [71]. The PL is then exclusively attributable to the presence of Eu^{3+} in the crystal lattice. Furthermore, the results demonstrate that temperature influences the Raman signals, which become more distinct as the reaction temperature rises, indicating enhanced crystallinity. Indeed, the spectra in Fig. 3a display very broad peaks, which are typical of materials with low crystallinity. In contrast, the spectra in Fig. 3b show peaks that are sharper and better shaped. The sample prepared at 160 °C shows an intermediate situation: the peaks are sharper than those of the amorphous samples, but larger than those of the samples prepared at higher temperatures (Fig. 3b, highlighted by red arrows). This indicates that the sample heated to 160 °C comprises a mixture of amorphous and crystalline phases, with a lower degree of crystallinity than observed in samples prepared at higher temperatures. These findings align with the XRD data, which indicate that the onset of crystallization for these materials prepared by microwave heating occurs at 160 °C. Furthermore, Fig. 3 illustrates that the water peaks are no longer present in the spectra of samples prepared at reaction temperatures of 200 °C and above. This suggests that essentially dry samples are obtained at higher temperatures, which is consistent with the results observed in the FT-IR spectra shown in Fig. 2. In addition, by employing the appropriate conversion of the wave number to the wavelength scale (see the experimental section for details), it is feasible to derive the wavelengths of the PL peaks and to assign the observed PL transitions by analogy with the data presented in the literature [48]. All known

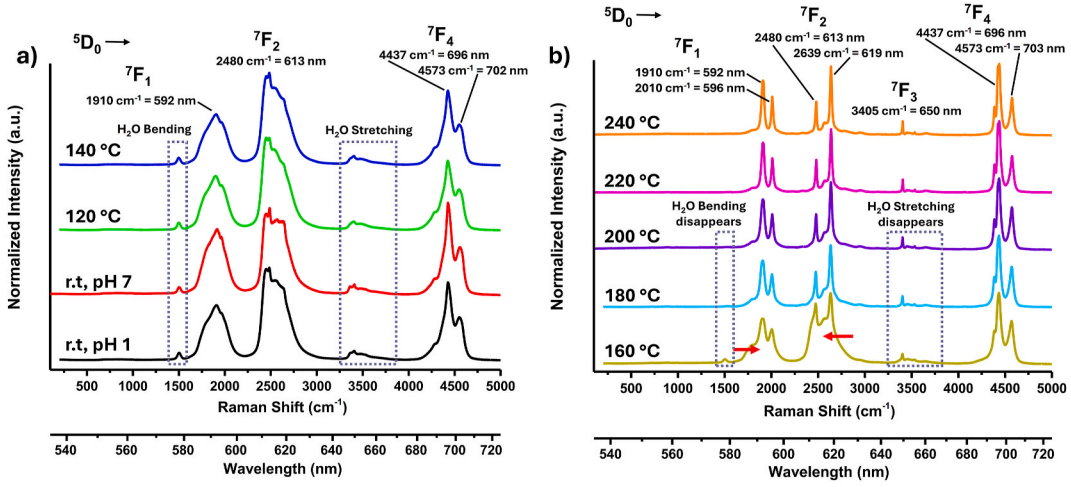

Fig. 3. Raman spectra of Eu^{3+}:YPO_4 nanopowders in the 100-5000 cm^{-1} range (**a**) Spectra obtained for samples synthesized at room temperature (black and red lines) and by the MW heating at T = 120 and 140 °C. (**b**) Spectra obtained for samples synthesized by the MW heating at T = 160–240 °C. The corresponding photoluminescence transitions are given, including the wavelength at which peaks maxima are observed and their corresponding Raman shifts. The wavelength scale corresponding to wavenumber scale is given below. (For interpretation of the references to colour in this figure legend, the reader is referred to the Web version of this article.)

transitions are observed in the spectra, with the exception of the weak $^7F_3$ peak at 3405 cm^{-1} (650 nm), which is only visible in dry samples. Wide-range Raman spectroscopy can therefore be a useful tool to provide preliminary information about the nature of the samples, qualitatively confirming their PL properties and relating them to their crystallinity and water content.

3.3. TEM analysis

The impact of temperature on the crystallization process and the evolution of crystal morphology was examined through transmission electron microscopy (TEM) analysis. Fig. 4 illustrates a selection of TEM micrographs of samples prepared at varying temperatures. The results indicate that nanopowders of homogeneous size are typically obtained, which corroborates the hypothesis that the growth rate is essentially uniform across all crystals. This is attributed to the narrow temperature distribution within the microwave (MW) apparatus [72].

The sample obtained at room temperature at pH = 1, i.e., immediately after the addition of KH_2PO_4 (**PHO_RT_1**), is predominantly amorphous (Fig. 4(a) and S4(a)). However, the presence of very small crystallites is discernible (Fig. S4(b)), exhibiting well-resolved lattice fringe spacing of approximately 3.5 Å, which is attributed to the (2 0 0) plane of the *Xenotime-Y* tetragonal phase (JCPDS: 00-011-0254, Fig. S4 (c)). The sample is devoid of any impurities (Fig. S4(f)) and its amorphous nature did not impede the uniform and homogeneous mixing of yttrium and europium, as evidenced by the EDS map and profile (Fig. S4 (d-e)). This indicates that Eu^{3+}:YPO_4 has already formed at this stage, albeit in an amorphous form. Similarly, the sample obtained at room temperature at pH = 7 also exhibits both amorphous and crystalline structures (Fig. S5(a-b)) with a homogeneous distribution of all elements (Fig. S5(c-f)), as previously reported in our recent paper [48]. These findings are corroborated by Raman analyses, which demonstrate the presence of characteristic bands associated with Eu^{3+} ions in spectra of specimen obtained without heat treatment, both at pH = 1 and under neutral conditions. However, this sample exhibits larger and more well-defined crystals with a rice-like morphology compared to the as-precipitated sample obtained under acidic conditions. These results substantiate the assertion that an initial crystallization process driven solely by a change in pH is active at room temperature. A pH effect is also observed by Garrido-Hernández et al., who claim that a low concentration of H_3O^+ is effective in promoting the formation of nanocrystals with anhydrous tetragonal structure [18]. The presence of a considerable fraction of the amorphous phase is evident in the samples obtained after MW treatment at 120 °C (Fig. 4(b) and S6(a-b)) and 140 °C (Fig. 4(c) and S6(a-b)). Nevertheless, the presence of Eu^{3+}:YPO_4 crystallized particles is also discernible, with larger crystals disappearing, indicating a dissolution/recrystallisation process [30]. This finding is corroborated by Select Area Diffraction (SAED, Fig. S6(c)). The sample prepared at 160 °C (Fig. 4d) exhibits a fairly well-defined morphology, in accordance with the results from XRD and Raman spectroscopy. Indeed, as can be seen in Fig. 5(a-e) and the size distributions shown in Fig. 5g-h, the powders are composed of nanobundles of approximately 30 nm thickness and 30–50 nm length, formed by very thin nanosticks (approximately 3 nm thickness). This is in good agreement with the crystallite size as calculated by the Rietveld refinement method (Table 1). In some areas, smaller nanosticks can be distinguished from amorphous areas, suggesting that the formation of nanobundles occurs via a two-step process: first, nanosticks are formed from amorphous material, and then they aggregate to form nanobundles. These results indicate that as the temperature is elevated, the amorphous powders undergo a gradual dissolution, followed by a rapid recrystallisation process, resulting in the formation of Eu^{3+}:YPO_4 crystalline nuclei as the temperature approaches 150–160 °C. The high crystallinity of the particles is corroborated by the selected area electron diffraction (SAED) patterns depicted in Fig. 5f, which exhibit the well-resolved (1 0 1), (2 0 0), (1 1 2), (3 1 2), (3 3 2) and (2 2 4) planes of the *Xenotime-Y* crystal phase (JCPS 00-011-0254, Table S1).

The homogeneity of the Eu^{3+} doping in the YPO_4 lattice and the purity of the material are confirmed by the EDS elemental maps, profile and spectrum presented in Fig. 6.

As the temperature increases to 180 °C (Fig. 4e and S8) and 200 °C (Fig. 4f), the nanobundles become more densely packed and aligned, with a reduction in the number of free nanosticks. In particular, at 200 °C, the densely packed structures appear as nanoparticles with non-uniform size and morphology, as observed in Ref. [48] The shape of the nanoparticles undergoes a transformation at the highest temperatures. At 220 and 240 °C, the original nanobundle structure is lost, and new morphologies emerge. As illustrated in Figs. 4(f) and **7**, at 220 °C, nanorods and cuboidal particles are formed, whereas at 240 °C, nanobullets with a homogeneous size (average length of 38 nm and thickness

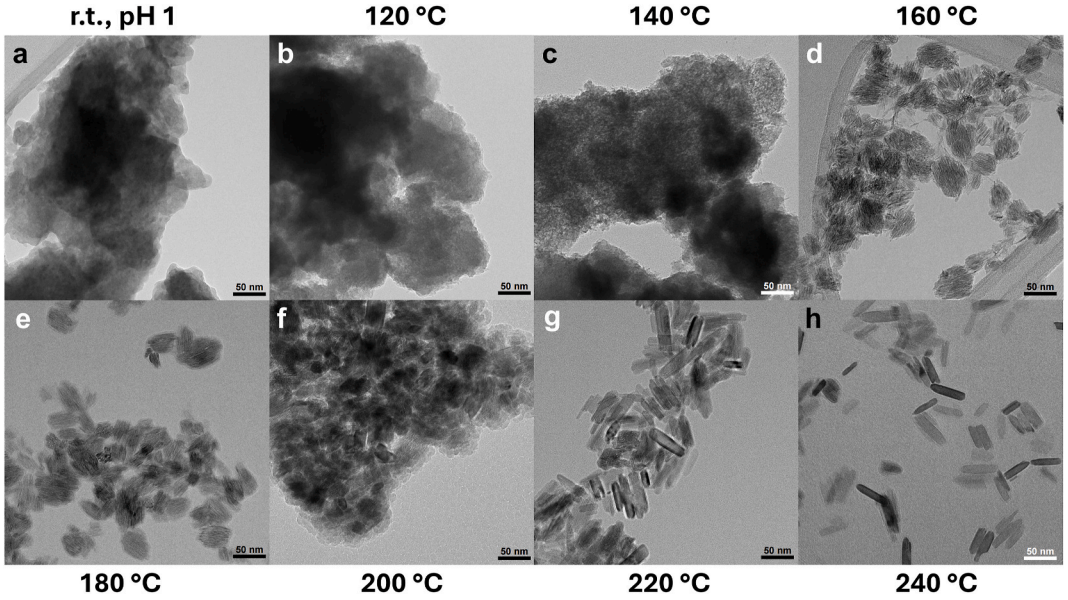

Fig. 4. TEM micrographs (at 150k magnification) of all Eu^{3+}:YPO_4 samples obtained after precipitation at room temperature at pH = 1 **(a)** and after 20 min of MW heating at 120 °C **(b)**, 140 °C **(c)**, 160 °C **(d)**, 180 °C **(e)**, 200 °C **(f)**, 220 °C **(g)** and 240 °C (**h**, from Ref. [48]).

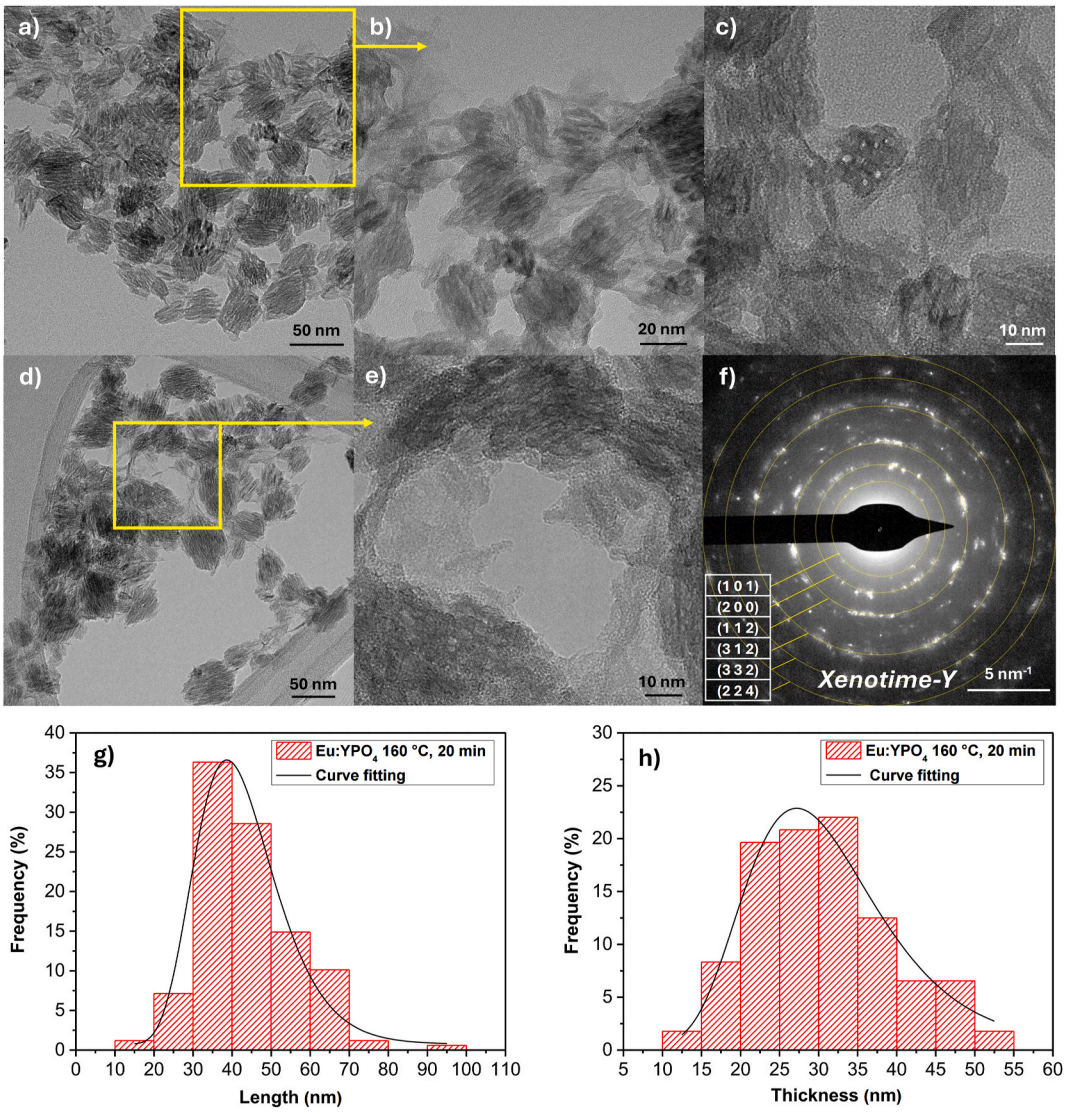

Fig. 5. (**a-e**) TEM micrographs at different magnifications of **PHO_160** sample and (**f**) SAED diffraction pattern with the indication of the crystal planes typical of the *Xenotime-Y* phase. The calculated interplanar distances are given in Table S1. (**g-h**) Size distribution in both directions, i.e., length and thickness.

of 11 nm) and morphology are obtained (Fig. 4h). It can be seen that as the temperature of the reaction increases, the initially formed nanosticks aggregate into nanobundles and then pack on top of each other until coalescence occurs. This is probably due to the dehydration process, and results in the formation of well-structured morphologies.

The quantitative EDS results for all samples are presented in Table S2. These results demonstrate no significant differences between the samples and exhibit good agreement with the theoretical values, with the exception of minor discrepancies within the instrumental errors.

The mean particle size values (mean length and thickness values) and aspect ratio, as determined from the TEM micrographs, are presented in Fig. 8(a) and 8(b), respectively. It is evident that the reaction temperature exerts a discernible influence on the dimensions of the nanoparticles, in alignment with the findings of the XRD analysis. In particular, the thickness decreases with increasing temperature, from 30 to 11 nm, while the aspect ratio values (length/thickness ratio) increase from 1.5 for the nanobundles to 3.2 and 3.5 for the more elongated rod- and bullet-shaped particles. There is a slight discrepancy between the dimensions measured from the TEM micrographs and the values given in Table 1, obtained from the XRD analysis, particularly for the samples obtained at the highest temperatures (220 and 240 °C). The nanopowders obtained at these elevated temperatures exhibit elongated rod and spherical morphologies with increased anisotropy compared to those obtained at lower temperatures. The discrepancies between the XRD crystallite sizes and the TEM measurements can be attributed to the methodology employed in calculating the crystallite sizes. The crystalline domains were determined using MAUD's Rietveld processing models, with Popa's rules applied and an average of the crystallite sizes extrapolated, which approximates an isotropic geometry. In particular, for the elongated particles, the crystallite size was calculated as an average between two directions. This is the reason for the tendency of the crystallite size to deviate partially from that of the particle length, especially for highly anisotropic geometries.

3.4. Proposed crystallization mechanism

Fig. 9 presents a schematic illustration of the crystallization and morphology evolution processes observed when the pH conditions were altered and the temperature was increased. The material is initially amorphous, but the addition of KOH at a pH of 7 results in the formation of relatively large nanocrystals. It can be seen that the pH value is of great importance in the process of crystallization, as evidenced by the formation of relatively large rice grains when the pH is altered. Zou et al.

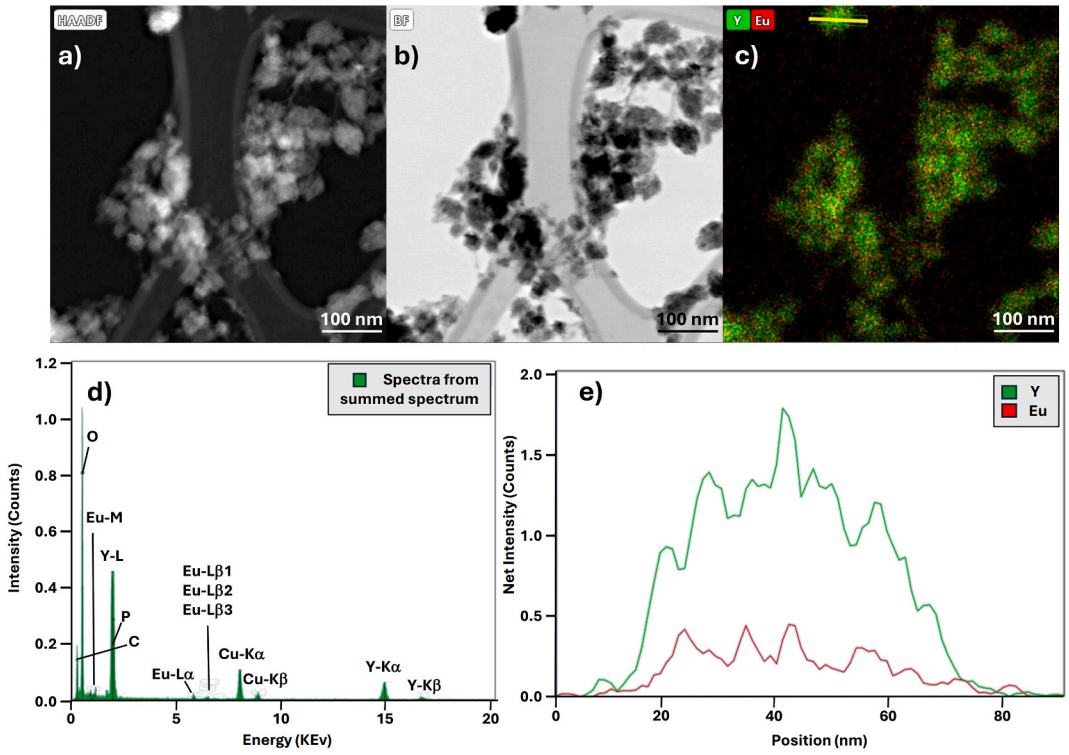

Fig. 6. HAADF (**a**) and BF (**b**), EDS elemental mapping (**c**), EDS spectrum (**d**) and profile (**e**) on Eu^{3+}:YPO_4 powders obtained at **160 °C**.

propose that under conditions of pH = 1 the phosphate anions would be almost absent from the solution, as the low pH favours the acidic form of H_3PO_4, which is less reactive and thus inhibits grain growth [15]. An increase in the pH of the solution has the effect of promoting partial deprotonation, resulting in the formation of higher concentrations of $H_2PO_4^-$, $HPO_4^{2-}$and free PO_4^{3-} in the reaction media. This, in turn, facilitates the crystallization process. Indeed, at a pH of 5 and in the absence of additives, tetragonal nanospindles of considerable dimensions were formed. Additionally, Gavrilović et al. observed the formation of nanorods (approximately 4 × 20 nm) at pH = 9 and a temperature of 60 °C in the coprecipitation synthesis of Eu^{3+}:$LaPO_4$. Their finding corroborates the hypothesis that these compounds crystallize in elongated morphologies under neutral conditions at low temperatures and in the absence of additives or organic solvents [13]. Furthermore, it has been reported that at elevated concentrations of PO_4^{3-}, the formation of the tetragonal *Xenotime-Y* phase is favoured over the hexagonal *Rhabdophane* structure [14]. Our results reveal that MW heating to temperatures of 120 and 140 °C yields a predominantly amorphous material, with only minute crystallites discernible. Conversely, the larger nanocrystals observed at room temperature are no longer visible. From these results, we can infer a possible dissolution-nucleation mechanism occurring in the initial stages of the reaction. This involves the rapid formation of nanocrystals at room temperature and pH = 7, which are then dissolved upon heating, giving rise to a second nucleation process occurring at high temperatures. Wu et al. have also proposed that this mechanism is active during the synthesis of Sm^{3+}:YPO_4, which was studied over time at pH = 3 and a reaction temperature of 200 °C [30]. We observed that an increase in reaction temperature resulted in the rapid growth of nanosticks and subsequent formation of nanobundles between 140 and 160 °C. This suggests that a crystallization threshold may be reached around 150 °C. In the paper by Yang et al., it was claimed that the use of glycine as an additive was crucial for obtaining Eu^{3+}:YPO_4 powders with nanobundle morphology by a conventional hydrothermal method [47]. The formation of nanobundles of comparable dimensions was also observed at the same temperature using a microwave-assisted synthesis devoid of organic additives, thereby indicating that the presence of glycine is not a prerequisite [45]. The aforementioned studies both synthesize nanobundles at 150 °C, utilising a reaction time of 24 h at an unspecified pH for the hydrothermal reaction and a duration of only 30 min at pH = 2 for the MW reaction. This evidence corroborates the assertion that the MW-assisted method yields identical outcomes to those of classical hydrothermal synthesis, albeit in a more expeditious manner. As the reaction temperature rises, the nanobundles become increasingly densely packed, culminating in the formation of well-defined nanorods and nanobullets at temperatures between 220 and 240 °C. This phenomenon may be exclusive to neutral conditions, as it is starkly divergent from the observations made at pH = 1. Indeed, Cybinska conducted a study on the morphological evolution of Eu^{3+}:YPO_4 as a function of temperature at pH = 1, wherein the formation of increasingly larger microparticles with cubic or octahedral morphology was observde, while maintaining the tetragonal crystal structure [32]. It can be hypothesised that the higher particle size values are favoured by low pH. Therefore, it can be proposed that in the case of RE^{3+}:YPO_4 phosphors, low pH favours slow nucleation and fast growth to give large microparticles, whereas neutral pH favours fast nucleation and slow growth to give small nanoparticles. These findings are consistent with the observations reported by Wang et al. in their study on the impact of tartrate anions on the crystallization of Ln^{3+}:YPO_4 [73]. The pH was found to exert a pronounced influence on the crystal phase, size and morphology. Indeed, large crystals were obtained at pH = 1, whereas small crystals were observed at pH values above 7. Two distinct growth mechanisms are proposed: at low pH, a direct nucleation/growth process is posited, whereas at higher pH, a dissolution-reprecipitation mechanism is proposed. Additionally, the authors hypothesize that at higher pH, the elevated concentration of PO_4^{3-} free anions facilitates rapid nucleation, thereby inhibiting the formation of large crystals and promoting the growth of smaller ones. As can be observed from the data presented in Table 1, an increase in reaction temperature is associated with a reduction in both the *a* and *c* parameters and the crystallite size. Furthermore, this observation can be correlated with the fast nucleation mechanism that was just discussed. It can be assumed that the higher the temperature, the higher the

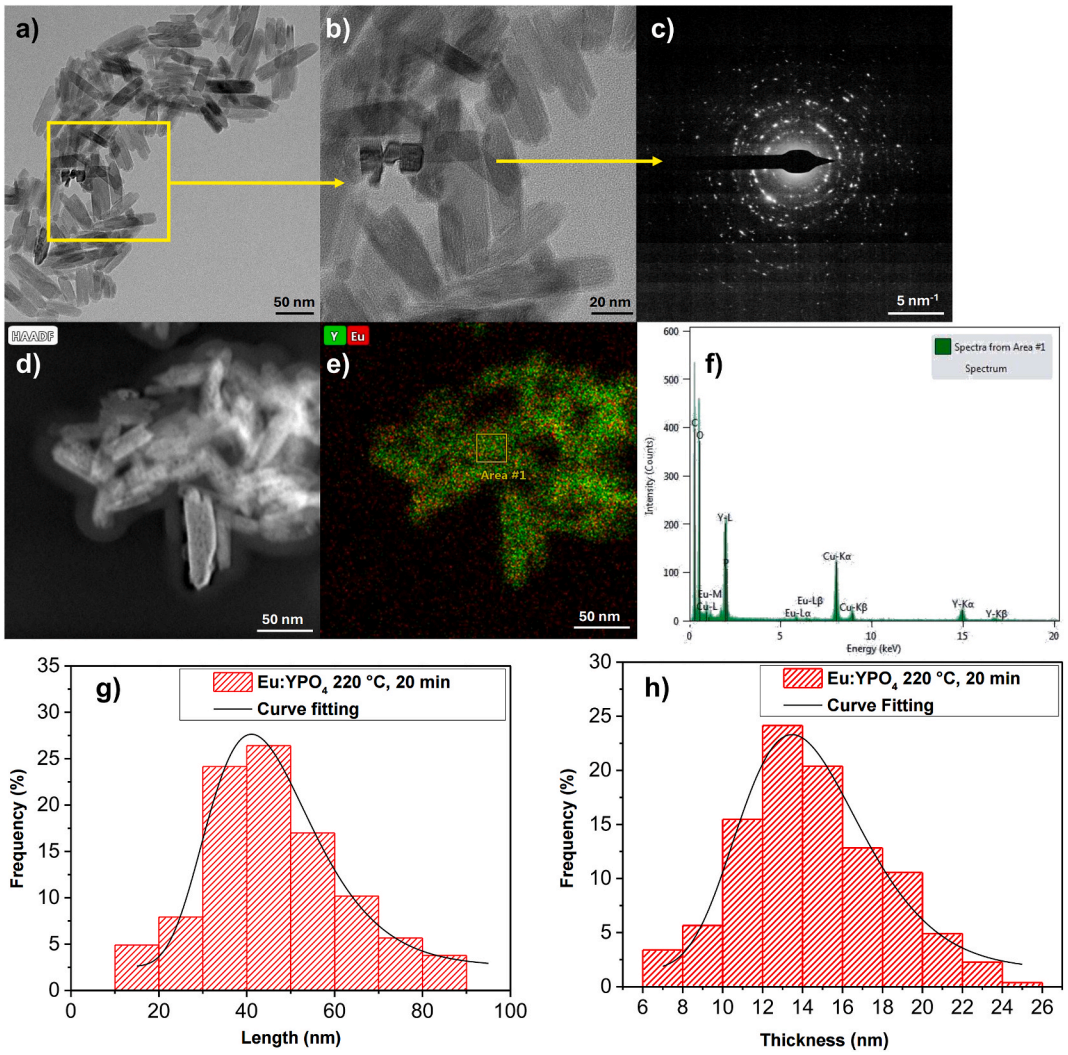

Fig. 7. (**a, b**) TEM micrographs at different magnifications of Eu^{3+}:YPO_4 nanopowders obtained at **220**. (**c**): selected area diffraction pattern (SAED). (**d**) HAADF (high-angle annular dark field) micrograph obtained in the STEM mode (**e**) Eu and Y elemental mapping and EDS spectrum (**f**) of the area highlighted in yellow in (**e**). (**g-h**) Size distribution in both directions, i.e., length and thickness. (For interpretation of the references to colour in this figure legend, the reader is referred to the Web version of this article.)

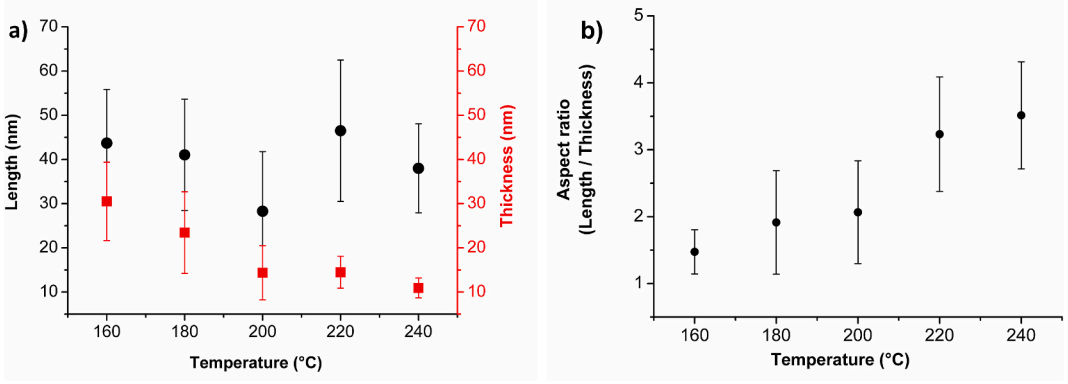

Fig. 8. **(a)** Mean particle size values (mean length and thickness values) and **(b)** aspect ratio (length/thickness ratio) determined by TEM micrographs for Eu^{3+}:YPO_4 nanopowders obtained at all different temperatures (data for samples prepared at 200 and 240 °C from Ref. [48]).

nucleation rate. In conclusion, it can be stated that at low temperatures, low pH does not favour crystallization; however, high pH triggers the process, resulting in the formation of elongated crystals of moderate size. Conversely, at higher temperatures (>160 °C), low pH allows the formation of very large crystals, whereas at higher pH, the fast nucleation process maintains the crystal size moderate. These observations and discussions are summarised in Fig. 9.

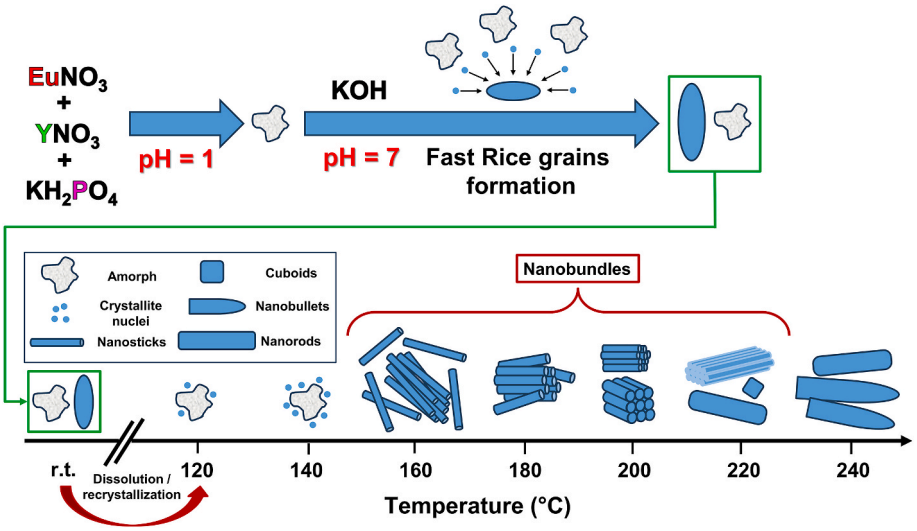

Fig. 9. Schematic representation of nanocrystal morphology changes as synthesis temperature is increased.

4. Conclusion

The objective of this study was to investigate the crystallization mechanism of Eu^{3+}:YPO_4 nanophosphors synthesized via a MW-assisted hydrothermal method in a safe and environmentally friendly manner, thereby addressing a gap in the existing scientific literature. Accordingly, the MW synthesis of Eu^{3+}:YPO_4 (5 % Eu) was conducted at pH = 7 in the absence of organic templates or solvents, with a fixed holding time of 20 min and varying reaction temperatures, including room temperature and a range between 120 and 240 °C. At the lowest temperatures, amorphous nanopowders were obtained, as evidenced by XRD, FT-IR, RAMAN and TEM analysis. Conversely, at higher temperatures, crystalline materials with a tetragonal *Xeontime-Y* crystal structure were formed. Furthermore, the doping of Eu^{3+} ions in the YPO_4 lattice was observed to be homogeneous and uniform across all samples. These findings indicate that a precise crystallization threshold exists for the formation of nanocrystalline Eu^{3+}:YPO_4, occurring between 140 and 160 °C. Above this threshold, nanocrystalline nanobundles are formed. The crystallization process is accompanied by a dehydration process, as evidenced by FT-IR analyses. The TEM analyses revealed the presence of relatively large crystals that had formed at pH 7 prior to heating. However, in the powders obtained at 120 and 140 °C, only extremely small crystallites remained, suggesting a dissolution/second nucleation mechanism at relatively low temperatures. Conversely, the formation of small elongated nanosticks and their subsequent aggregation into nanobundles was observed to occur at temperatures above 160 °C. Upon an increase in temperature, the residual amorphous material gradually diminishes, resulting in the formation of fully crystalline nanoparticles at temperatures exceeding 200 °C. As the temperature rises, the nanobundles exhibit a progressive tightening of the intermolecular bonds, ultimately leading to their coalescence at temperatures exceeding 200 °C. This process culminates in the formation of well-defined nanocrystals, characterised by a distinct morphology, such as nanorods or nanobullets.

The results demonstrate the significant impact of temperature on the crystallization of these luminescent materials in an aqueous environment at pH = 7, addressing a knowledge gap in the existing scientific literature. These findings are of considerable interest to the scientific community, given the growing use of luminescent materials in the optoelectronic industry. The development of rapid, reliable and environmentally friendly methods to produce powders with diverse morphologies is therefore a highly relevant and valuable area of research.

CRediT authorship contribution statement

Enrico Paradisi: Writing – original draft, Visualization, Validation, Investigation, Data curation, Conceptualization. **Cecilia Mortalò:** Writing – original draft, Validation, Methodology, Investigation, Conceptualization. **Valentina Zin:** Writing – review & editing, Investigation, Formal analysis, Data curation. **Silvia Maria Deambrosis:** Writing – review & editing, Supervision. **Mauro Zapparoli:** Investigation. **Enrico Miorin:** Writing – review & editing. **Cristina Leonelli:** Writing – review & editing, Supervision.

Declaration of competing interest

The authors declare that they have no known competing financial interests or personal relationships that could have appeared to influence the work reported in this paper.

Acknowledgements

No specific grants from public, commercial or not-for-profit funding bodies were received for this research. The authors would like to thank Dr. Cecilia Rossi and Dr. Jonathan Vinet (Interdepartmental Research Centre “CIGS”, University of Modena and Reggio Emilia) for their help with the XRD and Raman analyses respectively. The authors are grateful to Dr. Joe Cross for English spell check.

Appendix A. Supplementary data

Supplementary data to this article can be found online at https://doi.org/10.1016/j.ceramint.2024.12.144.

References

[1] W.R. Algar, M. Massey, K. Rees, R. Higgins, K.D. Krause, G.H. Darwish, W. J. Peveler, Z. Xiao, H.-Y. Tsai, R. Gupta, K. Lix, M.V. Tran, H. Kim, Photoluminescent nanoparticles for chemical and biological analysis and imaging, Chem. Rev. 121 (2021) 9243–9358, https://doi.org/10.1021/acs.chemrev.0c01176.

[2] I. Gupta, S. Singh, S. Bhagwan, D. Singh, Rare earth (RE) doped phosphors and their emerging applications: a review, Ceram. Int. 47 (2021) 19282–19303, https://doi.org/10.1016/j.ceramint.2021.03.308.

[3] S.K. Gupta, K. Sudarshan, R.M. Kadam, Optical nanomaterials with focus on rare earth doped oxide: a review, Mater. Today Commun. 27 (2021) 102277, https://doi.org/10.1016/j.mtcomm.2021.102277.

[4] M.K. Hossain, S. Hossain, M.H. Ahmed, M.I. Khan, N. Haque, G.A. Raihan, A review on optical applications, prospects, and challenges of rare-earth oxides, ACS Appl.

Electron. Mater. 3 (9) (2021) 3715–3746, https://doi.org/10.1021/acsaelm.1c00682.
[5] S. Thakur, N. Dhiman, A. Sharma, A.K. Gathania, Effect of photonic structure on optical properties of YVO_4:Eu^{3+} phosphor, J. Electron. Mater. 46 (2017) 2085–2089, https://doi.org/10.1007/s11664-016-5133-x.
[6] S. Thakur, A. K Gathania, Optical properties of YVO_4:Eu^{3+} nano-phosphors at different europium concentrations, Indian J. Phys. 89 (2015) 973–979, https://doi.org/10.1007/s12648-015-0670-3.
[7] S. Chong, B.J. Riley, X. Lu, J. Du, T. Mahadevan, V. Hegde, Synthesis and properties of anhydrous rare-earth phosphates, monazite and xenotime: a review, RSC Adv. 14 (2024) 18978–19000, https://doi.org/10.1039/d4ra01142b.
[8] A.V. Popov, Y.V. Orlovskii, A.S. Vanetsev, O.M. Gaitko, E.O. Orlovskaya, I. Sildos, Nanosecond fluctuation kinetics of luminescence hopping quenching originated from the $5d^1$ level in the Ce^{3+}:$YPO_4{\cdot}0.8H_2O$ nanocrystals, J. Lumin. 145 (2014) 774–778, https://doi.org/10.1016/j.jlumin.2013.08.065.
[9] W. Di, X. Wang, B. Chen, S. Lu, X. Zhao, Effect of OH^- on luminescent efficiency and lifetime of Tb^{3+}-doped yttrium orthophosphate synthesized by solution precipitation, J. Phys. Chem. B 109 (2005) 13154–13158, https://doi.org/10.1021/jp051894i.
[10] E.V. Samsonova, A.V. Popov, A.S. Vanetsev, K. Keevend, E.O. Orlovskaya, V. Kiisk, S. Lange, U. Joost, K. Kaldvee, U. Mäeorg, N.A. Glushkov, A.V. Ryabova, I. Sildos, V.V. Osiko, R. Steiner, V.B. Loschenov, Y.V. Orlovskii, An energy transfer kinetic probe for OH^-quenchers in the Nd^{3+}:YPO_4 nanocrystals suitable for imaging in the biological tissue transparency window, Phys. Chem. Chem. Phys. 16 (2014) 26806–26815, https://doi.org/10.1039/C4CP03774J.
[11] P. Li, Y. Liu, Y. Guo, X. Shi, G. Zhu, H. Zuo, Hydrothermal synthesis of YPO_4:Eu^{3+} hexagonal prisms microarchitectures: tunable morphology, formation mechanism, and recovery luminescence properties, Ceram. Int. 41 (2015) 6620–6630, https://doi.org/10.1016/j.ceramint.2015.01.109.
[12] M. Niraj Luwang, R.S. Ningthoujam, Jagannath, S.K. Srivastava, R.K. Vatsa, Effects of Ce^{3+} codoping and annealing on phase transformation and luminescence of Eu^{3+}-doped YPO_4 nanorods: D_2O solvent effect, J. Am. Chem. Soc. 132 (2010) 2759–2768, https://doi.org/10.1021/ja909578s.
[13] T. Gavrilović, J. Periša, J. Papan, K. Vukivič, K. Smits, D.J. Jovanovič, M. D. Dramićanin, Particle size effects on the structure and emission of Eu^{3+}:$LaPO_4$ and $EuPO_4$, J. Lumin. 195 (2018) 420–429, https://doi.org/10.1016/j.jlumin.2017.12.002.
[14] P. Li, Y. Zhang, L. Zhang, F. Li, Y. Guo, Y. Li, W. Gao, Phase control of Eu^{3+}-doped YPO_4 nano-/microcrystals, Cryst. Growth Des. 17 (2017) 5935–5944, https://doi.org/10.1021/acs.cgd.7b01038.
[15] J. Zou, Q. Zu, X. Li, X. Sun, J.-G. Li, Controlled hydrothermal processing of multiform $(Y_{0.95}Eu_{0.05})PO_4$ crystals and comparison of photoluminescence, J. Alloys Compd. 870 (2021) 159380, https://doi.org/10.1016/j.jallcom.2021.159380.
[16] R. Priya, R. Mariappan, A. Karthikeyan, E. Palani, E. Krishnamoorth, G. Gowrisankar, Review on rare earth metals doped $LaPO_4$ for optoelectronic applications, Solid State Commun. 339 (2021) 114457, https://doi.org/10.1016/j.ssc.2021.114457.
[17] F. Armetta, V. Boiko, D. Hreniak, C. Mortalò, C. Leonelli, L. Barbata, M.L. Saladino, Effect of the hydrothermal time on the forming specific morphology of YPO_4:Eu^{3+} nanoparticles for dedicated luminescent applications as optical markers, Ceram. Int. 49 (2023) 23287–23294, https://doi.org/10.1016/j.ceramint.2023.04.159.
[18] A. Garrido Hernández, A. García Murillo, J. Reyes Miranda, J. Carrillo Romo de, F. Structural, Morphological, and luminescent properties of tetragonal-phase YPO_4: Eu^{3+}, Opt. Mater. 115 (2021) 111020 https://doi.org/10.1016/j.optmat.2021.111020.
[19] X. Li, H. Wang, L. Guan, Y. Fu, Z. Guo, K. Yuan, L. Tie, Z. Yang, F. Teng, Influence of pH value on properties of YPO_4:Tb^{3+} phosphor by Co-precipitation method, J. Rare Earths 33 (2015) 346–349, https://doi.org/10.1016/S1002-0721(14)60424-5.
[20] K. Srinivasu, R.S. Ningthoujam, V. Sudarsan, R.K. Vatsa, A.K. Tyagi, P. Srinivasu, A. Vinu, Eu^{3+} and Dy^{3+} doped YPO_4 nanoparticles: low temperature synthesis and luminescence studies, J. Nanosci. Nanotechnol. 9 (2009) 3034–3039, https://doi.org/10.1166/jnn.2009.026.
[21] R. Kahouadji, L. Guerbous, A. Boukerika, S.D. Dolić, D.J. Janović, Intra- and inter-configurational luminescence spectroscopy of Pr^{3+} -doped YPO_4 nanophosphors *Current Applied Physics*, 18, 437-446, https://doi.org/10.1016/j.cap.2018.01.012, 2018.
[22] B. Kahouadji, L. Guerbous, D.J. Jovanović, M.D. Dramićánin, M. Samah, L. Lamiri, M.M. Cincović, Annealing effect on the photoluminescence properties of Ce^{3+} doped YPO_4 nanophosphors, Opt. Mater. 91 (2019) 35–41, https://doi.org/10.1016/j.optmat.2019.02.052.
[23] J. Huang, R. Gao, Z. Lu, D. Qian, W. Li, B. Huang, X. He, Sol−gel preparation and photoluminescence enhancement of Li^+ and Eu^{3+} Co-doped YPO4 nanophosphors, Opt. Mater. 32 (2010) 857–861, https://doi.org/10.1016/j.optmat.2009.12.011.
[24] R. Kahouadji, L. Guerbous, D.J. Jovanović, M.D. Dramićánin, A.H. Souici, Photoluminescence properties of nano-sized $(Lu_{1-x}Y_x)PO_4$:Pr^{3+} (x = 10, 20, 30, 40, 50 at. %) phosphor powders, Opt. Mater. 109 (2020) 110252, https://doi.org/10.1016/j.optmat.2020.110252.
[25] H. Lai, Y. Du, M. Zhao, K. Sun, L. Yang, Effects of different organic additives on the Formation of YPO_4:Eu^{3+} nano-/microstructures under hydrothermal conditions with enhanced photoluminescence, Ceram. Int. 40 (2014) 1885–1891, https://doi.org/10.1016/j.ceramint.2013.07.094.
[26] M. Tan, S. Hao, X. Meng, J. Liu, Y. Shang, C. Yang, G. Chen, pH mediated control synthesis of lanthanide-doped YPO_4 upconversion nano/microcrystals, Am. J. Eng. Appl. Sci. 8 (3) (2015) 310–317, https://doi.org/10.3844/ajeassp.2015.310.317.
[27] H.F. Devi, T.D. Singh, Morphology control synthesis and photoluminescence of yttrium orthophosphate microstructures, Mater. Lett. 231 (2018) 8–10, https://doi.org/10.1016/j.matlet.2018.07.143.
[28] Y. Ge, X. Sun, Controllable synthesis and luminescence of YPO_4:ln^{3+} (Ln = Eu and Sm) nanotubes, J. Mater. Sci. Mater. Electron. 27 (2016) 6690–6696, https://doi.org/10.1007/s10854-016-4616-0.
[29] K. Chanchan, S. Dorendrajit Singh, Concentration effect on the luminescent and structural properties of YPO_4:Eu^{3+}, Mater. Today: Proc. 65 (2022) 2480–2483, https://doi.org/10.1016/j.matpr.2022.04.055.
[30] J. Wu, M. Li, H. Jia, Z. Liu, H. Jia, Z. Wang, Morphology Formation mechanism and fluorescence properties of nano-phosphor YPO_4:Sm^{3+} excited by near-ultraviolet light, J. Alloys Compd. 821 (2020) 153535, https://doi.org/10.1016/j.jallcom.2019.153535.
[31] Q. Liu, Y. Su, H. Yu, W. Han, YPO_4 nanocrystals: preparation and size-induced lattice symmetry enhancement, J. Rare Earths 26 (4) (2008) 495–500, https://doi.org/10.1016/S1002-0721(08)60125-8.
[32] J. Cybińska, Temperature dependent morphology variation of red emitting microcrystalline YPO_4:Eu^{3+} fabricated by hydrothermal method, Opt. Mater. 65 (2017) 88–94, https://doi.org/10.1016/j.optmat.2016.10.018.
[33] J.M. Nedelec, D. Avignant, R. Mahiou, Soft chemistry routes to YPO_4-based phosphors: dependence of textural and optical properties on synthesis pathways, Chem. Mater. 14 (2) (2002) 651–655, https://doi.org/10.1021/cm010572y.
[34] R. Krishnan, S.N. Shibu, D. Poelman, A.K. Badyal, A.K. Kunti, H.C. Swart, S. G. Menon, Recent advances in microwave synthesis for photoluminescence and photocatalysis, Mater. Today Commun. 32 (2022) 103890, https://doi.org/10.1016/j.mtcomm.2022.103890.
[35] J.M. de Carvalho, C.C. Santos Pedroso, M.S. de Nichile Saula, M.C.F. Cunha Felinto, H.F. de Brito, Materials: a fast route to light conversion and storage phosphors, Molecules 26 (2021) 2882, https://doi.org/10.3390/molecules26102882.
[36] V. Riva, D. Boccaccini, M. Cannio, M. Maioli, M. Valle, M. Romagnoli, C. Mortalò, C. Leonelli, Insight into *t*->*m* transition of MW treated 3Y-PSZ ceramics by grazing incidence X-ray diffraction, J. Eur. Ceram. Soc. 42 (2022) 227–237, https://doi.org/10.1016/j.jeurceramsoc.2021.09.054.
[37] C. Mortalò, R. Rosa, P. Veronesi, S. Fasolin, V. Zin, S.M. Deambrosis, E. Miorin, G. Dimitrakis, M. Fabrizio, C. Leonelli, Microwave assisted sintering of Na-β''-Al_2O_3 in single mode cavities: insights in the use of 2450 MHz frequency and preliminary experiments at 5800 MHz, Ceram. Int. 46 (2020) 28767–28777, https://doi.org/10.1016/j.ceramint.2020.08.039.
[38] E. Paradisi, R. Rosa, G. Baldi, V. Dami, A. Cioni, G. Lorenzi, C. Leonelli, Microwave–assisted vacuum synthesis of TiO_2 nanocrystalline powders in one–pot, one–step procedure, Nanomaterials 12 (2022) 149, https://doi.org/10.3390/nano12010149.
[39] E. Paradisi, C. Mortalò, P. Russo, V. Zin, E. Miorin, F. Montagner, C. Leonelli, S. M. Deambrosis, Facile and effective method for the preparation of sodium alginate/TiO_2 bio-composite films for different applications, Macromol. Symp. 413 (2024) 2300230, https://doi.org/10.1002/masy.202300230.
[40] P. Parhi, V. Manivannan, Novel microwave initiated solid-state metathesis synthesis and characterization of lanthanide phosphates and vanadates, LMO_4 (L = Y, La and M = V, P), Solid State Sci. 10 (2008) 1012–1019, https://doi.org/10.1016/j.solidstatesciences.2007.11.038.
[41] M.O. Enikeeva, O.V. Proskurina, D.P. Danilovich, V.V. Gusarov, Formation of nanocrystals based on equimolar mixture of lanthanum and yttrium orthophosphates under microwave-assisted hydrothermal synthesis, Nanosyst: Phys, Chem, Math 11 (2020) 705–715, https://doi.org/10.17586/2220-8054-2020-11-6-705-715.
[42] Z. Wang, Q. Zu, X. Shi, X. Wang, Q. Zhu, J.-G. Li, Unprecedented rapid synthesis of $REPO_4$ monospheres (RE=La-Lu lanthanide and Y) and investigation of multi-color photoluminescence, Chem. Eng. J. 343 (2018) 16–27, https://doi.org/10.1016/j.cej.2018.02.122.
[43] Q. Zhu, Z. Xu, Z. Wang, X. Wang, X. Li, X. Sun, J.-G. Li, Multi-color emission in monodispersed spheres of tetragonal yttrium phosphate: microwave-assisted fast synthesis, formation mechanism, temperature-dependent luminescence, and application in anti-fake labeling, CrystEngComm 20 (2018) 3187–3201, https://doi.org/10.1039/C8CE00365C.
[44] S. Rodriguez-Liviano, F.J. Aparicio, T.C. Rojas, A.B. Hungría, L.E. Chinchilla, M. Ocaña, Microwave-assisted synthesis and luminescence of mesoporous RE-doped YPO_4 (RE = Eu, Ce, Tb, and Ce + Tb) nanophosphors with lenticular shape, Cryst. Growth Des. 12 (2012) 635–645, https://doi.org/10.1021/cg201358c.
[45] S. Majeed, M. Bashir, S.A. Shivashankar, Dispersible crystalline nanobundles of YPO_4 and Ln (Eu, Tb)-Doped YPO_4: rapid synthesis, optical properties and bio-probe applications, J. Nanopart. Res. 17 (2015) 309, https://doi.org/10.1007/s11051-015-3113-3.
[46] A.S. Vanetsev, E.V. Samsonova, O.M. Gaitko, K. Keevend, A.V. Popov, U. Mäeorg, H. Mändar, I. Sildos, Y.V. Orlovskii, Phase composition and morphology of nanoparticles of yttrium orthophosphates synthesized by microwave-hydrothermal treatment: the influence of synthetic conditions, J. Alloys Compd. 639 (2015) 415, https://doi.org/10.1016/j.jallcom.2015.03.125.
[47] X. Yang, X. Dong, J. Wang, G. Liu, Glycine-assisted hydrothermal synthesis of YPO_4:Eu^{3+} nanobundles, Mater. Lett. 63 (2009) 629–631, https://doi.org/10.1016/j.matlet.2008.12.004.
[48] E. Paradisi, C. Mortalò, V. Zin, F. Armetta, V. Boiko, D. Hreniak, M. Zapparoli, S. M. Deambrosis, E. Miorin, C. Leonelli, M.L. Saladino, Eu-doped YPO_4 luminescent nanopowders for anticounterfeiting applications: tuning morphology and optical properties by a rapid microwave-assisted hydrothermal method, ACS Appl. Nano Mater. 7 (2024) 6893–6905, https://doi.org/10.1021/acsanm.3c05806.

[49] L. Lutterotti, Total pattern fitting for the combined size-strain-stress-texture determination in thin film diffraction, Nucl. Instrum. Methods Phys. Res. 268 (2010) 334–340, https://doi.org/10.1016/j.nimb.2009.09.053. *B*.

[50] L. Lutterotti, D. Chateigner, S. Ferrari, J. Texture Ricote, Residual stress and structural analysis of thin films using a combined X-ray analysis, Thin Solid Films 450 (2004) 34–41, https://doi.org/10.1016/j.tsf.2003.10.150.

[51] L. Lutterotti, M. Bortolotti, G. Ischia, I. Lonardelli, H.-R. Wenk, Rietveld texture analysis from diffraction images, Z. Kristallogr. Suppl. 26 (2007) 125–130, https://doi.org/10.1524/9783486992540-020.

[52] N.C. Popa, D. Balzar, Size-broadening anisotropy in whole powder pattern fitting. Application to zinc oxide and interpretation of the apparent crystallites in terms of physical models, J. Appl. Crystallogr. 41 (2008) 615–627, https://doi.org/10.1107/S0021889808012223.

[53] C. Mortalò, A. Santoru, C. Pistidda, E. Rebollo, M. Boaro, C. Leonelli, M. Fabrizio, Structural evolution of $BaCe_{0.65}Zr_{0.20}Y_{0.15}O_{3-\delta}$-$Ce_{0.85}Gd_{0.15}O_{2-\delta}$ composite MPEC membrane by in-situ synchrotron XRD analyses, Mater. Today Energy 13 (2019) 331–341, https://doi.org/10.1016/j.mtener.2019.06.004.

[54] P. Muhammed Shafi, E. Kurian, N. Joseph, S. Sellaiyan, A. Uedono, A. Chandra Bose, Effect of Ag doping on crystallinity and microstrain of $LaMnO_3$ nanoparticles: confirmations of defect levels with positron lifetime and Doppler-broadening calculations, Phys. B Condens. Matter 615 (2021) 413087, https://doi.org/10.1016/j.physb.2021.413087.

[55] Y. Wu, Z. Zhang, H. Suo, X. Zhao, C. Guo, 808 nm light triggered up-conversion optical nano-thermometer YPO_4:Nd^{3+}/Yb^{3+}/Er^{3+} based on FIR technology, J. Lumin. 214 (2019) 116578, https://doi.org/10.1016/j.jlumin.2019.116578.

[56] H. Farida Devi, T.H. Singh, Morphology control synthesis and luminescence of yttrium orthophosphate microstructures, Mater. Lett. 231 (2018) 8–10, https://doi.org/10.1016/j.matlet.2018.07.143.

[57] Z. Wang, J.-G. Li, Q. Zhu, X. Li, X. Sun, Hydrothermal conversion of layered hydroxide nanosheets into $(Y_{0.95}Eu_{0.05})PO_4$ and $(Y_{0.96-x}Tb_{0.04}Eu_x)PO_4$ ($x = 0$–0.10) nanocrystals for red and color-tailorable emission, RSC Adv. 6 (2016) 22690–22699, https://doi.org/10.1039/C6RA00434B.

[58] Z. Yahiaoui, M.A. Hassairi, M. Dammak, Synthesis and optical spectroscopy of YPO_4:Eu^{3+} orange–red phosphors, J. Electron. Mater. 46 (8) (2017) 4765–4773, https://doi.org/10.1007/s11664-017-5401-4.

[59] E. Stavrou, A. Tatsi, E. Salpea, Y.C. Boulmetis, A.G. Kontos, Y.S. Raptis, C. Raptis, Raman study of zircon-structured RPO_4 (R = Y, Tb, Er, Tm) phosphates at high pressures, J. Phys. Conf. Ser. 121 (2008) 042016, https://doi.org/10.1088/1742-6596/121/4/042016.

[60] L.A. Zavala-Sanchez, G.A. Hirata, E. Novitskaya, K. Karandikar, M. Herrera, O. A. Graeve, Distribution of Eu^{2+} and Eu^{3+} ions in hydroxyapatite: a cathodoluminescence and Raman study, ACS Biomater. Sci. Eng. 1 (2015) 1306–1313, https://doi.org/10.1021/acsbiomaterials.5b00378.

[61] A.K. Gulnar, V. Sudarsan, R.K. Vatsa, T. Sakuntala, A.K. Tyagi, U.K. Gautam, A. Vinu, Nucleation sequence on the cation exchange process between $Y_{0.95}Eu_{0.05}PO_4$ and $CePO_4$ nanorods, Nanoscale 2 (2010) 2847–2854, https://doi.org/10.1039/C0NR00334D.

[62] F. Baldassarre, A. Altomare, N. Corriero, E. Mesto, M. Lacalamita, G. Bruno, A. Sacchetti, B. Dida, D. Karaj, G. Della Ventura, F. Capitelli, D. Siliqi, Crystal chemistry and luminescence properties of Eu-doped polycrystalline hydroxyapatite synthesized by chemical precipitation at room temperature, Crystals 10 (2020) 250, https://doi.org/10.3390/cryst10040250.

[63] Only one example reported very small in a larger graphics was found in C. Lenz, L. Nasdala, D. Talla, C. Hauzenberger, R. Seitz, U. Kolitsch, Laser-induced REE^{3+} photoluminescence of selected accessory minerals — an "advantageous artefact" in Raman spectroscopy, Chem. Geol. 415 (2015) 1–16, https://doi.org/10.1016/j.chemgeo.2015.09.001.

[64] A. Kassiba, M. Makowska-Janusik, J. Boucle, J.F. Bardeau, A. Bulou, N. Herlin-Boime, Photoluminescence features on the Raman spectra of quasistoichiometric SiC nanoparticles: experimental and numerical simulations, Phys. Rev. B 66 (2002) 155317, https://doi.org/10.1103/PhysRevB.66.155317.

[65] J.J. Goedhart, T.P. Kuipers, V.M. Papadakis, Raman and photoluminescence signal separation in Raman hyperspectral imagery including noise reduction, J. Raman Spectrosc. 55 (2024) 598–614, https://doi.org/10.1002/jrs.6651.

[66] L. Cabo-Fernandez, A.R. Neale, F. Braga, I.V. Sazanovich, R. Kostecki, L. J. Hardwick, Kerr gated Raman spectroscopy of $LiPF_6$ salt and $LiPF_6$-based organic carbonate electrolyte for Li-ion batteries, Phys. Chem. Chem. Phys. 21 (2019) 23833–23842, https://doi.org/10.1039/c9cp02430a.

[67] S. Mosca, C. Conti, N. Stone, P. Matousek, Spatially offset Raman spectroscopy, Nat. Rev. Methods Primers 1 (2021) 21, https://doi.org/10.1038/s43586-021-00019-0.

[68] D. Wei, S. Chen, Q. Liu, Review of fluorescence suppression techniques in Raman spectroscopy, Appl. Spectrosc. Rev. 50 (5) (2015) 387–406, https://doi.org/10.1080/05704928.2014.999936.

[69] D. Tuschel, Photoluminescence spectroscopy using a Raman spectrometer, Spectroscopy 31 (9) (2016) 14–21.

[70] T. Seki, K.-Y. Chiang, C.-C. Yu, X. Yu, M. Okuno, J. Hunger, Y. Nagata, M. Bonn, The bending mode of water: a powerful probe for hydrogen bond structure of aqueous systems, J. Phys. Chem. Lett. 19 (2020) 8459–8469, https://doi.org/10.1021/acs.jpclett.0c01259.

[71] N. Clavier, A. Mesbah, S. Szenknect, N. Dacheux, Rhabdophane Monazite, Xenotime & churchite: vibrational spectroscopy of gadolinium phosphate polymorphs, Spectrochim. Acta: Mol. Biomol. Spectrosc. 205 (2018) 85–94, https://doi.org/10.1016/j.saa.2018.07.016.

[72] C. Ponzoni, R. Rosa, M. Cannio, V. Buscaglia, E. Finocchio, P. Nanni, C. Leonelli, Optimization of BFO microwave-hydrothermal synthesis: influence of process parameters, J. All. Comp. 558 (2013) 150–159, https://doi.org/10.1016/j.jallcom.2013.01.039.

[73] Z. Wang, J.-G. Li, Q. Zhu, B.-N. Kim, X. Sun, Dicarboxylate mediated efficient morphology/phase tailoring of YPO_4:Ln^{3+} crystals and investigation of down-/up-conversion luminescence, CrystEngComm 19 (2017) 5230–5243, https://doi.org/10.1039/C7CE01248A.